Modeling nonlinearities of ultrasonic waves for fatigue damage characterization: Theory, simulation, and experimental validation

Ming Hong [a,b], Zhongqing Su [a,b,*], Qiang Wang [c], Li Cheng [a,b], Xinlin Qing [d]

[a] The Hong Kong Polytechnic University, Shenzhen Research Institute, Shenzhen 518057, PR China
[b] Department of Mechanical Engineering, The Hong Kong Polytechnic University, Kowloon, Hong Kong
[c] College of Automation, Nanjing University of Posts and Telecommunications, Nanjing, PR China
[d] Division of Aviation Health and Safety Management, Beijing Aeronautical Science and Technology Research Institute COMAC, Beijing 100083, PR China

ABSTRACT

A dedicated modeling technique for comprehending nonlinear characteristics of ultrasonic waves traversing in a fatigued medium was developed, based on a retrofitted constitutive relation of the medium by considering the nonlinearities originated from material, fatigue damage, as well as the "breathing" motion of fatigue cracks. Piezoelectric wafers, for exciting and acquiring ultrasonic waves, were integrated in the model. The extracted nonlinearities were calibrated by virtue of an acoustic nonlinearity parameter. The modeling technique was validated experimentally, and the results showed satisfactory consistency in between, both revealing: the developed modeling approach is able to faithfully simulate fatigue crack-incurred nonlinearities manifested in ultrasonic waves; a cumulative growth of the acoustic nonlinearity parameter with increasing wave propagation distance exists; such a parameter acquired via a sensing path is nonlinearly related to the offset distance from the fatigue crack to that sensing path; and neither the incidence angle of the probing wave nor the length of the sensing path impacts on the parameter significantly. This study has yielded a quantitative characterization strategy for fatigue cracks using embeddable piezoelectric sensor networks, facilitating deployment of structural health monitoring which is capable of identifying small-scale damage at an embryo stage and surveilling its growth continuously.

© 2013 Elsevier B.V. All rights reserved.

1. Introduction

Effectual damage evaluation and continuous health monitoring are conducive to reliable service of engineering structures, and the risk of structural failure can accordingly be minimized. Taking advantage of appealing features including high sensitivity to structural damage, omnidirectional dissemination, fast propagation, and strong penetration through thickness, ultrasonic waves have been a subject of intense scrutiny over the years, with demonstrated compromise between conventional non-destructive evaluation (NDE) and emerging structural health monitoring (SHM) [1–7]. Predominantly, deployment of this group of techniques is often based on exploring changes in the linear wave scattering upon the interaction of incident probing waves with structural damage. These changes can be manifested in acquired ultrasonic wave signals, typified as delay in time-of-flight, wave attenuation, and mode conversion. These signal features, for example the delay in time-of-flight, show, to some extent, linear correlations with damage parameters such as location, and are therefore referred to as *linear features*.

However, it is a corollary that linear features-based detection is fairly limited to the evaluation of damage with a size on the same order of the magnitude of the probing wavelength [8], presenting inefficiency in perceiving fatigue damage which often initiates at an unperceivable level much smaller than the probing wavelength. This is because the damage of small dimension is not anticipated to induce evident changes in linear features to be extracted from ultrasonic waves [9]. This situation has posed immediate urgency and entailed imperative needs for exploring other wave signal features that can be prominently modulated by small-scale damage, so as to endow the ultrasonic inspection with a capability of scrutinizing damage small in dimension and fatigue cracks in particular.

Nonlinear ultrasonic interrogation has emerged under such a demand. More specifically, instead of extracting and canvassing linear signal properties, the nonlinear ultrasonic inspection attempts to quantify the nonlinear distortion of probing waves due to the damage, for instance the generation of higher-order harmonics. Such a detection philosophy has ushered a new avenue of using ultrasonic waves to predict fatigue damage at an embryo stage prior to the formation of gross damage detectable by linear techniques.

* Corresponding author at: Department of Mechanical Engineering, The Hong Kong Polytechnic University, Kowloon, Hong Kong. Tel.: +852 2766 7818; fax: +852 2365 4703.
  E-mail address: MMSU@polyu.edu.hk (Z. Su).

There has been a rich body of literature on the use of nonlinear features of ultrasonic waves [9–16]. Most of existing research strength has been in a nature of experimental observation on possible changes in nonlinear properties of probing waves, primarily Lamb waves (the modality of elastic waves in thin plate- or shell-like structures) [10–13]. There are rather limited studies devoted to the analytical investigation or numerical simulation of nonlinear ultrasonic waves propagating in fatigued media. Among representative numerical methods to simulate nonlinearities of media and/or damage are Local Interaction Simulation Approach (LISA) [14], finite element method (FEM) [15], and Galerkin FEM [16].

In general, a paramount challenge in analytically or numerically modeling nonlinear ultrasonic waves in a fatigued medium is the comprehensive inclusion of all possible sources of nonlinearities from both the medium itself and the damage, as well as the interpretation on the modulation mechanism of fatigue damage on ultrasonic waves. Aimed at a systematic comprehension of the nonlinear natures of ultrasonic waves in a medium bearing fatigue damage, this study is dedicated to the establishment of a modeling technique — supplemented with experimental validation — that is capable of producing and interpreting nonlinearities in ultrasonic waves. Instead of using bulky wedge probes that are commonly adopted in prevailing nonlinear ultrasonic interrogation, miniaturized piezoelectric wafer sensors, which can be flexibly networked and permanently attached to the structure under inspection, are utilized, benefiting extension of the approach to embeddable SHM.

This paper is organized as follows: Section 2 discusses the origins of nonlinearities in an elastic medium, serving as the cornerstone of the study, residing on which the modeling technique for an ideally intact medium and its fatigued counterpart is developed. An acoustic nonlinearity parameter is established to quantitatively calibrate the captured nonlinearity. By integrating identified sources of nonlinearities, Section 3 models the nonlinear properties manifested in ultrasonic waves traversing in a metallic medium featuring introduced nonlinearities. Section 4 embraces implementation of the modeling through finite element (FE) simulation, and signal processing for extracting nonlinearities from ultrasonic wave signals. Case studies using the developed modeling technique are presented in Section 5, investigating the dependence of the acoustic nonlinearity parameter on wave propagation distance, on sensing path offset from a fatigue crack, and on wave incidence angle. Finally, Section 6 renders concluding remarks.

2. Modeling nonlinearities in an elastic medium

Consider an isotropic homogeneous solid with purely elastic behavior, the nonlinearities of the medium that may contribute to nonlinear distortion of its guided ultrasonic waves can originate from different sources, including mainly the material, the damage-driven plasticity, the loading conditions, to name a few.

2.1. Intact state

When the medium is in an ideally intact state (no fatigue damage existent), two nonlinearity sources are accountable: the inherent material nonlinearity and the geometric nonlinearity, with the former from the intrinsic nonlinear elasticity of the medium (*viz.*, the elasticity of lattices). Usually, lattice vibrations in a metallic medium are assumed to obey simple harmonic motion and the material is assumed to be pristine (*i.e.*, no precipitates or vacancies). This assumption is largely applicable for engineering applications in the domain of linear elasticity. However, in reality there is always lattice anharmonicity (referring to the crystal vibrations that do not follow the simple harmonic motion), and/or there are

precipitates and vacancies in the material. These nonlinearity effects, though trivial, can be manifested by ultrasonic waves propagated in such a medium.

In the domain of nonlinear elasticity, the three-dimensional stress–strain relation for the above solid medium can be depicted, with a second-order approximation, as follows [17]

$$\sigma_{ij} = (C_{ijkl} + 1/2 M_{ijklmn}\varepsilon_{mn})\varepsilon_{kl}, \tag{1}$$

where σ_{ij} is the stress tensor; ε_{mn} and ε_{kl} are the strain tensors; C_{ijkl} and such in its form in the succeeding equations are the second-order elastic (SOE) tensors defined with Lamé parameters λ_L and μ; M_{ijklmn} is a tensor associated with the material and geometric nonlinearities. If the second term in the parenthesis, $1/2 M_{ijklmn}$, is neglected, Eq. (1) reverts to the three-dimensional Hooke's Law of linear elasticity.

In the meantime, the geometric nonlinearity is closely related to the material nonlinearity. Generally, wave motion equations are written in Eulerian (spacial) coordinates, while nonlinear elasticity in solids is formulated in Lagrangian (material) coordinates. For linear elasticity, these two coordinate systems do not differ from each other; nevertheless, given the material nonlinearity taken into account, a descriptive difference emerges, starting from the second-order term of any physical quantity involved [18]. In simpler words, geometric nonlinearity is induced mainly due to the mathematic transform between two coordinate systems. Hence, tensor M_{ijklmn} in Eq. (1) addresses both the material and geometric nonlinearities simultaneously, which can be expressed in terms of the notation by Landau and Lifshitz [19] as follows

$$M_{ijklmn} = C_{ijklmn} + C_{ijln}\delta_{km} + C_{jnkl}\delta_{im} + C_{jlmn}\delta_{ik} \tag{2}$$

where

$$C_{ijklmn} = \frac{1}{2}\mathcal{A}(\delta_{ik}I_{jlmn} + \delta_{il}I_{jkmn} + \delta_{jk}I_{ilmn} + \delta_{jl}I_{ikmn}) + 2\mathcal{B}(\delta_{ij}I_{klmn} + \delta_{kl}I_{mnij} + \delta_{mn}I_{ijkl}) + 2\mathcal{C}\delta_{ij}\delta_{kl}\delta_{mn}. \tag{3}$$

In Eqs. (2) and (3), δ_{km} and such in its form with different index orders are the Kronecker deltas; I_{jlmn} and such in its form are the fourth-order identity tensors. C_{ijklmn} is the third-order elastic (TOE) tensor describing the material nonlinearity, and the last three terms in Eq. (2) all together address the geometric nonlinearity. As shown in Eq. (3), C_{ijklmn} is determined by three TOE constants $\mathcal{A}$, $\mathcal{B}$ and $\mathcal{C}$, which can be regarded as the inherent properties of the material, to be measured experimentally [20,21]. C_{ijklmn} can further be expressed explicitly with Voigt notation in terms of the three TOE constants, as

$$\begin{cases} c_{111} = 2\mathcal{A} + 6\mathcal{B} + 2\mathcal{C} \\ c_{112} = 2\mathcal{B} + 2\mathcal{C} \\ c_{123} = 2\mathcal{C} \\ c_{144} = 1/2\mathcal{A} + \mathcal{B} \\ c_{155} = \mathcal{B} \\ c_{456} = 1/4\mathcal{A}, \end{cases} \tag{4}$$

where $c_{IJK} = C_{ijklmn}$ ($I, J, K \in \{1, 2, \ldots, 6\}$). For example, the cases for $I = 1, 2, \ldots, 6$ correspond to those when $ij = 11, 22, 33, 12, 23, 31$, respectively, and any other scalar components of C_{ijklmn} falls into the six cases defined by Eq. (4).

For generality, first consider a one-dimensional medium, such as a rod, which can be governed by the one-dimensional nonlinear stress–strain equation as follows:

$$\sigma = (E + E_2\varepsilon)\varepsilon, \tag{5}$$

where σ, ε, E, and E_2 are the stress, strain, and the first- and second-order Young's moduli of the medium, respectively. E reflects the

linear properties, whereas E_2 introduces the nonlinear effects [22] to the medium. Solving Eqs. (1)–(3) yields

$$E_2 = -\frac{1}{2}(3E + 2\mathcal{A} + 6\mathcal{B} + 2\mathcal{C}) \tag{6}$$

Further, take the ratio of the two Young's moduli

$$\beta_g = \frac{E_2}{E} = -\frac{1}{2}\left(3 + \frac{2A + 6B + 2C}{E}\right) \tag{7}$$

In this study, β_g defined by Eq. (7) is referred to as the *global nonlinearity parameter* of the medium. Obviously, β_g is dominated by four material property parameters (Young's modulus and three TOE constants) provided the medium contains, ideally, no fatigue damage or plastic deformation. Thus β_g can be regarded as a material property to quantify the intrinsic nonlinearities of the medium.

2.2. Fatigued state

For a medium bearing fatigue damage, there are additional sources of nonlinearities in the vicinity of the damage besides β_g. Fatigue damage initially appears in the form of microstructure defects such as dislocations. Under repetitive loading, dislocations accumulate and form persistent slip bands (PSBs), which, at the grain boundaries, nucleate microcracks on the scale of millimeters. Finally, microcracks coalesce and grow into macroscopic cracks that propagate through the material. Because the number of loading cycles it takes to produce a macroscopic crack leading to structural failure is much smaller than the number to initiate microcracks, it is of vital importance to detect fatigue cracks before a microcrack forms. In what follows, we limit the discussion to the nonlinearities presented in the early stage of fatigue damage up to the point when PSB walls emerge.

For low-cycle fatigue (LCF), since the loading stress is larger than the yield strength of the material, bulk plastic deformation takes place, which is not homogeneous; instead it is expected to locally concentrate in the vicinity of the fatigue damage [23]. On the other hand, for high-cycle fatigue (HCF), with primarily elastic deformation, localized micro-plastic deformation also exists in the region of crack initiation. Therefore, for both LCF and HCF, localized plasticity is present in the vicinity of crack initiation due to dislocations and slips, both distorting guided waves and introducing nonlinear properties to wave signals.

To reflect the localized plasticity above, a *local nonlinearity parameter* β_l is defined, in contrast to β_g, to account for the plasticity-induced nonlinearity incurred by fatigue damage. β_l reads, for a dislocation dipole setting [24], as

$$\beta_l = \frac{16\pi\Omega R^2 \Lambda h^3 (1-\nu)^2 (\lambda_L + 2\mu)^2}{\mu^2 b}, \tag{8}$$

where Ω and R are two factors of conversions from dislocation to longitudinal, and from longitudinal to shear displacements, respectively; Λ is the dipole dislocation density associated with the plastic strain of the medium, h the dipole height, ν the Poisson's ratio, and b the Burgers vector. Usually, the nonlinearity due to micro-plastic deformation contributes more significantly to the nonlinear distortion of ultrasonic waves than intrinsic material nonlinearity does [12,13].

Taking both the global and local nonlinearity parameters into account, a *hybrid acoustic nonlinearity parameter* β is constructed in this study, up to the point when PSB walls with plastic strains are produced, as

$$\beta = \begin{cases} \beta_g, & \text{Intact state} \\ \beta_g + \beta_l. & \text{Damaged state due to local plasticity} \end{cases} \tag{9}$$

Once a localized plasticity is introduced to the structure, β is increased owing to β_l only in the vicinity of the fatigue damage, while in the rest of the material it remains unchanged as β_g. This local change provides a theoretical basis for quantitative characterization of fatigue damage in virtue of captured β.

2.3. Contact acoustic nonlinearity

In addition to β, as the fatigue deterioration continues to the point when microcracks are physically nucleated with sufficient accumulation of dislocations, the *contact acoustic nonlinearity* (CAN) also needs to be addressed: when ultrasonic waves traverse the interface between two surfaces of a microcrack, the "breathing" motion pattern of the crack under cyclic loading closes the gap during wave compression, in which compressive and shear stresses are transmitted, according to the "breathing crack model" [25]; when tension opens the crack, tensile stress cannot be transmitted. Since various stress–strain relations exist across the crack depending on whether it is open or closed, their superposition imposes an additional localized nonlinearity, CAN, to the signals of ultrasonic waves guided by the medium [26]. Moreover, other factors such as roughness of the crack surfaces, friction, thermal effects, and partial closure may also present, more or less, nonlinearities and contribute to variations in CAN. With such complexity, there has been a lack of means to theoretically relate CAN to the ultrasonic wave responses in terms of β [26]. However, CAN could be conveniently modeled to approach the reality, which is discussed in Section 4.

3. Modeling nonlinearities in ultrasonic waves

3.1. Longitudinal waves

Continuing discussion on the above one-dimensional medium, we consider the longitudinal waves in the medium first. By neglecting dispersion and attenuation, the motion equation for the guided waves in the Lagrangian coordinates is formulated as

$$\rho \frac{\partial^2 u(x,t)}{\partial t^2} = \frac{\partial \sigma}{\partial x}, \tag{10}$$

where ρ is the density of the medium, $u(x,t)$ the particle displacement at x along propagation direction at instant t (abbreviated as u in what follows). Having discussed the nonlinear stress–strain relation in a one-dimensional isotropic homogeneous solid, wave responses in this medium can be obtained by solving Eqs. (5) and (10) simultaneously in virtue of a perturbation theory [22]. The yielded particle displacement u has a zero-order solution at the excitation frequency ω, plus a first-order perturbation solution at the double frequency 2ω, as

$$u = A_1 \cos(kx - \omega t) + A_2 \cos(2kx - 2\omega t), \tag{11}$$

where k is the wavenumber, ω the angular frequency of excitation, and A_1 and A_2 the magnitudes of the fundamental wave mode at ω, and the second harmonic wave mode at 2ω, respectively. The two magnitudes are linked to each other by $A_2 = 1/8\ \hat{\beta}A_1^2 k^2 x$, where $\hat{\beta}$ denotes the *acoustic nonlinearity parameter*, to be obtained via either experimentation or simulation. It reads, after rearrangement,

$$\hat{\beta} = \frac{8}{k^2 x} \frac{A_2}{A_1^2}. \tag{12}$$

It is noteworthy that $\hat{\beta}$ is not always equal to the ideally modeled β defined by Eq. (9) under all circumstances, particularly when there are physical fatigue cracks presented. That is because some types of nonlinearities, such as CAN, are not analytically included in the stress–strain model as discussed in Section 2, which,

nonetheless, also contribute to the generation of higher-order harmonics and can be reflected by the measured $\hat{\beta}$. Thus, the actual change in $\hat{\beta}$ due to local plasticity and emerging microcracks, determined via either experimentation or simulation, should in general be larger than the value of β_l as analytically obtained via Eq. (8), in which only micro-plastic deformation is considered. Yet, previous works [9,12,13] have demonstrated that an increase in β due to the presence of plasticity-driven fatigue damage can be adequately, if not exactly, represented by the change in $\hat{\beta}$.

Based on Eq. (12), the degree of nonlinearity associated with the material and the fatigue damage can be determined by probing the magnitudes of the fundamental and its corresponding second harmonic modes. In order to detect the damage, one may be more interested in the change in $\hat{\beta}$ rather than its absolute value; therefore, at a fixed wave propagation distance with certain wavenumber, the acoustic nonlinearity parameter can be normalized with respect to its initial value in the intact state of the medium, yielding a *relative acoustic nonlinearity parameter*, β', to quantify the degree of *change* of the nonlinearities of ultrasonic waves, as

$$\beta' = \frac{A_2}{A_1^2}. \tag{13}$$

This relatively defined nonlinearity parameter is proportional to β and contains essential information reflecting the nonlinear properties of wave propagation. Thus, it can serve as a primary index to be monitored for quantitative characterization of fatigue damage.

3.2. Lamb waves

Lamb waves are highly dispersive and multimodal, with multiple modes propagating simultaneously at different velocities through all excitation frequencies, particularly at higher ones. The dispersive nature of Lamb waves makes the generation of higher-order harmonics and their measurement a challenging task, compared to the case for longitudinal waves aforementioned. Nevertheless, their second harmonics can become significant and cumulative when particular fundamental modes are excited at deliberately selected frequencies, which simultaneously meet the conditions of *synchronism* and *non-zero power flux* [10]. Specifically, synchronism refers to the phase velocity matching and group velocity matching between the excited fundamental mode and the accordingly generated second harmonic mode, respectively and concurrently [12,13]. This matching warrants power transfer from the fundamental to the second harmonic mode of the same mode type (either both are symmetrical or both are antisymmetric) smoothly, resulting in cumulative generation of the second harmonic mode along wave propagation.

For illustration, Fig. 1 displays the dispersion curves calculated using DISPERSE® for Lamb waves in an aluminum plate from zero through 10 MHz·mm. Mode pair (S_1, S_2) is an option to accommodate both synchronism and non-zero power flux, hence called a *synchronized mode pair* hereinafter, of which S_1, the first-order symmetric Lamb mode at the frequency-thickness product of 3.57 MHz·mm, and S_2, the second-order symmetric Lamb mode at 7.14 MHz·mm, propagate at the same phase and group velocities, respectively. Therefore, when S_1 mode is excited in a plate of uniform thickness (along with other modes excited at that frequency), S_2 mode is expected to be generated at twice the excitation frequency, being the corresponding second harmonic of S_1. Owing to the same phase and group velocities, generation of the second harmonic mode is cumulative along wave propagation.

Extending the discussion from the one-dimensional medium to a plate-like medium guiding Lamb waves, the acoustic nonlinearity parameter for longitudinal waves can be redefined for Lamb waves
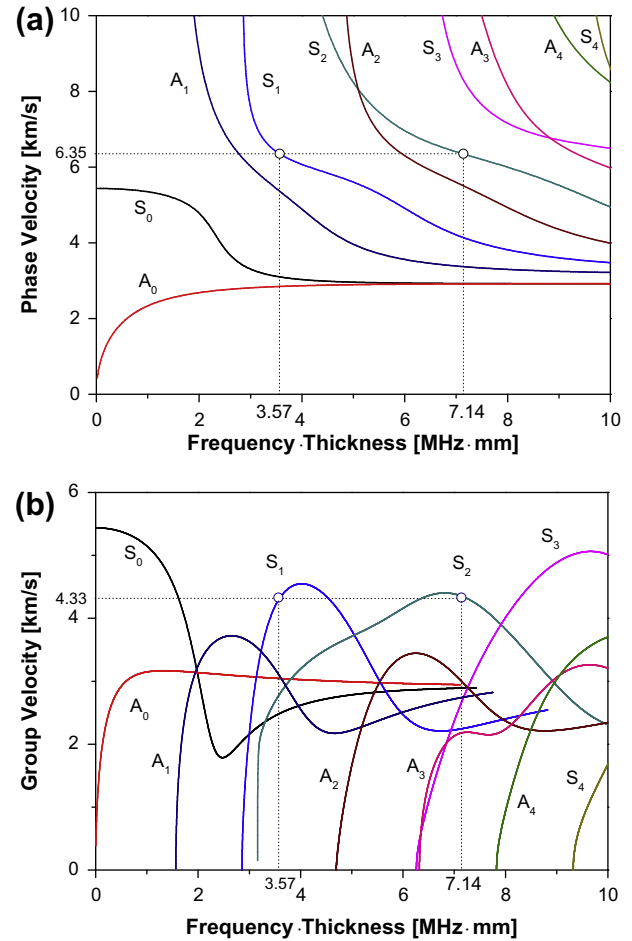
Fig. 1. Dispersion curves of Lamb waves propagating in an aluminum plate calculated using DISPERSE®: (a) phase velocity vs. frequency-thickness and (b) group velocity vs. frequency-thickness (circled are a synchronized mode pair (S_1, S_2)).

by multiplying Eq. (12) with a scaling factor γ, which is a function depending on Lamb wave factors and medium properties [27], as

$$\hat{\beta}_{Lamb} = \frac{8}{k^2 x} \frac{A_2}{A_1^2} \gamma. \tag{14}$$

$\hat{\beta}_{Lamb}$ signifies the acoustic nonlinearity parameter for Lamb waves. Allowing for the fact that a plate has an unchanged γ before and after the occurrence of fatigue damage, and following the normalization process of $\hat{\beta}$ as detailed earlier for the one-dimensional medium, γ can be eliminated and thus the relative nonlinearity parameter β', from Eq. (13), alone is sufficient to characterize fatigue damage in the plate.

4. Implementation of modeling

Based upon the above discussions on nonlinearities in the medium (when it is in intact and fatigued states) and on nonlinear guided ultrasonic waves, a dedicated modeling technique is developed and realized in conjunction with the commercial FEM software Abaqus®/EXPLICIT. All possible sources of nonlinearities including CAN, as introduced in the above, are taken into account in the modeling.

The modeling of material, geometric, and plasticity-driven nonlinearities is achieved by introducing a modified nonlinear stress–strain relation to Abaqus®/EXPLICIT through user

subroutine VUMAT, which is specifically used for material definition. For the material and geometric nonlinearities that exist homogeneously in the medium, material constants including density, Young's modulus, and TOE constants are passed in the modeling; for the plasticity-driven nonlinearity, an extra local nonlinearity parameter is added to the global nonlinearity parameter in the vicinity of the fatigue damage (by calling a second set of property values in the same VUMAT subroutine). As the simulation is dynamic in nature, *Forward Euler* procedure (explicit integration) is used in VUMAT to transform the constitutive rate equation, defined according to Eq. (1), to an incremental equation. A two-state architecture is adopted, so that variables such as the strain increment and stress increment have their initial values in old arrays and updated values in new arrays in each iteration. Taking advantage of the explicit integration, these variables are all vectorized to facilitate computing process. In order to maintain the simulation stability, time increment is controlled to warrant convergence of calculation. Moreover, considering the magnitude of deformation that can be induced by a piezoelectric lead zirconate titanate (PZT) wafer (to be used in succeeding experimental validation), double precision is specified in simulation to ensure computation accuracy.
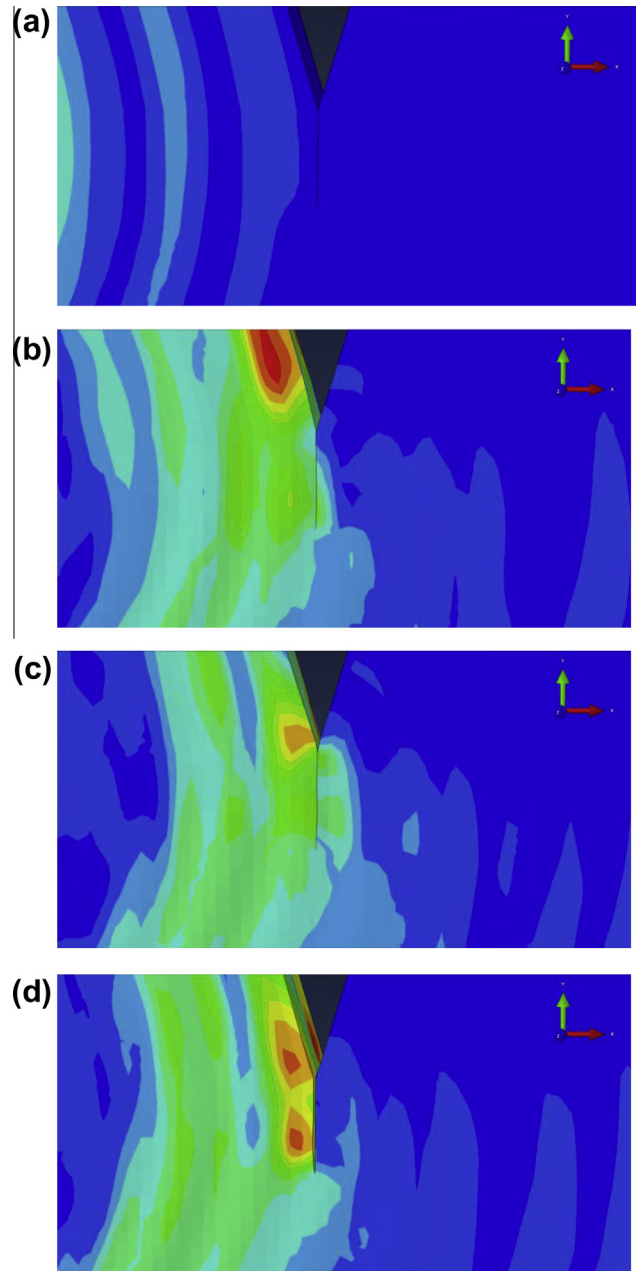
To model a fatigue crack in the medium, a seam crack definition is imposed on each surface of the crack, as illustrated in Fig. 2, to enable the breathing behavior when waves traverse the crack. Furthermore, a contact-pair interaction and associated properties are defined on the crack interface to supplement the modeling of CAN. Fig. 3a–d demonstrate the process of ultrasonic Lamb waves traversing a breathing crack. It can be clearly seen that the stress induced by Lamb wave propagation is continuously transmitted through the crack when it is closed (Fig. 3b and c), while on the contrary an open crack interrupts the transmission process (Fig. 3d).

Using the above modeling technique, case studies are performed and analyzed (to be detailed in the next section). As a representative, Fig. 4 shows the time-domain presentation of a typical Lamb wave signal. In order to extract the required signal features
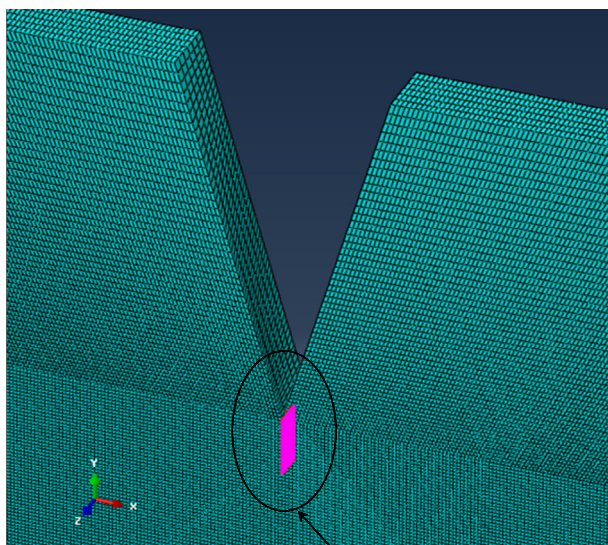
Fig. 3. Snapshots of ultrasonic waves traversing a fatigue crack with CAN in modeling: (a) waves approaching the crack; (b) stress starting to traverse the crack when it is closed; (c) stress transmitting through the closed crack and (d) stress being blocked when the crack is open.

Fig. 2. A fatigue crack created near a notch tip in a meshed plate in Abaqus® (highlighted regions are the two crack surfaces with the seam crack definition and contact-pair properties).

to construct β', short-time Fourier transform (STFT) is performed on the time-domain signal, with the obtained spectrogram shown in Fig. 5. The window size of STFT is carefully chosen such that sufficient details of both time and frequency information of the signal could be retained. From the spectrogram, one can extract the amplitude profiles at fundamental and double frequencies as a respective function of time. In accordance with Fig. 1, it is obvious that both the fundamental mode S_1 and its second harmonic mode S_2 are the first arrivals at their corresponding frequencies. Thus, the first peak value of the amplitude profile at the fundamental frequency is identified as A_1 (of S_1 mode), and the first peak value of the amplitude profile at the second harmonic frequency as A_2 (of S_2 mode), as illustrated in Fig. 6. Consequently, β' associated with this particular signal can be calculated using Eq. (13).
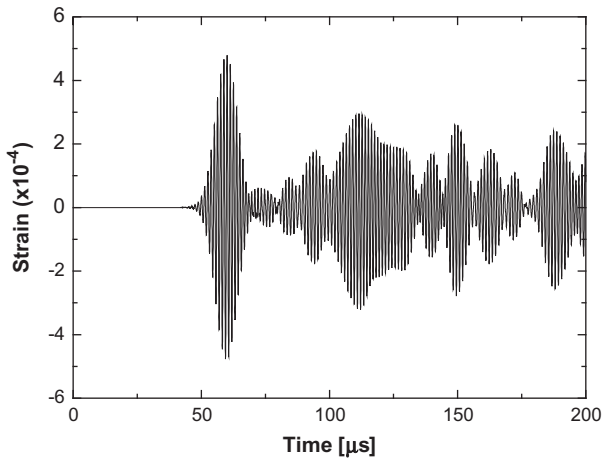
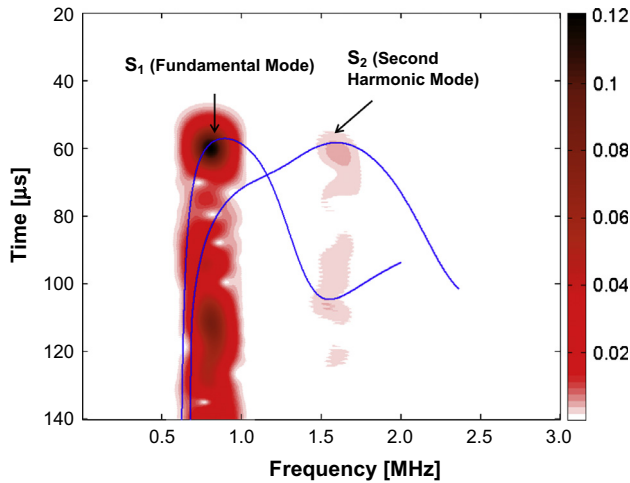**Fig. 4.** Time-domain presentation of a typical lamb wave signal acquired in simulation.

Fig. 5. Time–frequency spectrogram of signal in Fig. 4 obtained via STFT, integrated with the dispersion curves of S_1 and S_2 modes.
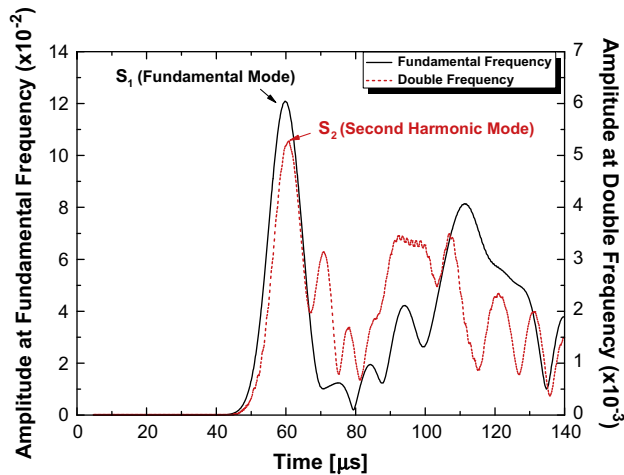

Fig. 6. Amplitude profiles of the signal energy at the fundamental frequency and at the double frequency.

5. Validation and discussions

The proposed modeling technique was verified by case studies, followed with experimental validation.

5.1. β' vs. propagation distance

The change in β' subject to wave propagation distance in an undamaged plate medium was interrogated first. The rationale of this test is: when a synchronized mode pair is excited, β' extracted from captured ultrasonic Lamb wave signals is expected to be proportional to wave propagation distance, provided the medium remains in an ideally healthy state.

Using the developed modeling approach, a 6061 aluminum plate ($400 \times 380 \times 4.5$ mm^3), shown schematically in Fig. 7a, was modeled. The three-dimensional nonlinear elastic stress–strain relation described by Eq. (1) was recalled to define material properties through VUMAT, introducing both the material and geometric nonlinearities. The SOE constants (Lamé parameters λ_L and μ) can be calculated from the material's Young's modulus (68.9 GPa in this case) and Poisson's ratio (0.33). The TOE constants of the aluminum used in all case studies are: $A = -320$ GPa, $B = -200$ GPa and $C = -190$ GPa [20]. Three-dimensional eight-node brick elements (C3D8R) in Abaqus® were used to mesh the plate through a structured meshing algorithm. All the elements were equally sized at 0.25 mm in the in-plane dimensions to ensure at least 20 elements per wavelength of the fundamental wave mode S_1, and 10 per wavelength of S_2, to warrant simulation precision; nine elements were assigned along the plate thickness. Nine circular PZT wafers were assumed to be on the same side of the plate, each of which had a nominal diameter of 8 mm and a thickness of 0.5 mm. These PZT wafers served, respectively, as a wave actuator (A) and eight sensors (S_I – S_{VIII}), hence configuring eight actuator-sensor paths. Deliberate positioning of the nine PZT wafers led to a wave propagation distance d_i ($i = I, II\ldots VIII$) between A and S_i ranging from 60 to 200 mm in an increment of 20 mm, with actuator-sensor path $A – S_I$ being the shortest (60 mm) and $A – S_{VIII}$ the longest (200 mm), as shown in Fig. 7a. PZT wafers were modeled by creating a disc-like object comprising four elements. Along each actuator-sensor path, five-cycle Hann-windowed sinusoidal tone bursts at 800 kHz were excited by imposing uniform in-plane radial displacements on the nodes along periphery of the actuator model, as illustrated in Fig. 7b. The excitation frequency of 800 kHz enabled the generation of S_1 mode as the fundamental wave mode in accordance with Fig. 1 (considering the plate thickness is 4.5 mm). Dynamic simulation was performed, and wave signals were acquired at locations of the eight sensors in the form of in-plane elemental strains.

The same configuration was used in the experiment to validate the above modeling. Nine PZT wafers were individually surface-mounted through a thin adhesive layer on a damage-free 6061 aluminum plate as shown in Fig. 7c, and then connected to a signal generation and acquisition system developed on a *VXI* platform [28]. Shielded wires and standard BNC connectors were adopted to reduce measurement noise. The same excitation signal as in the simulation was generated by Agilent E1441 waveform generator, and then amplified by a US-TXP-3 linear power amplifier to 100 V$_{p-p}$ before it was applied on the PZT actuator. Lamb wave signals were acquired by the eight PZT sensors through Agilent E1438 signal digitizer at a sampling rate of 100 MHz.

STFT-based signal processing as described in Section 4 was recalled to obtain the relative acoustic nonlinearity parameter β' associated with each sensing path, in accordance with Eq. (13). The relationships of β' vs. propagation distance obtained from the modeling and the experiment are displayed in Figs. 8a and 8b, respectively. Note that β' features a unit of strain in simulation, but V^{-1} in the experiment. It can be seen that both relationships reveal a quasi-linear cumulative growth of β' over propagation distance, confirming that the nonlinearity manifested in a captured ultrasonic Lamb wave signal is essentially from the intrinsic nonlinearity of the medium as anticipated previously. The consistency
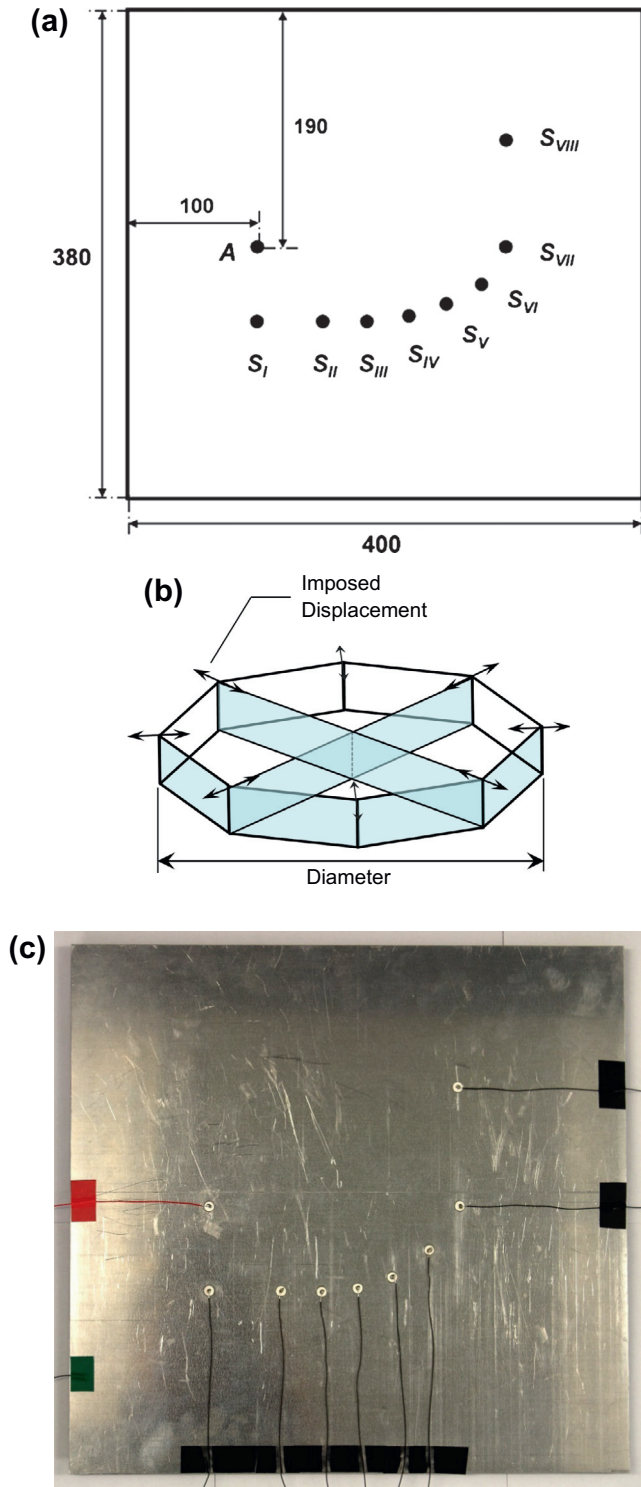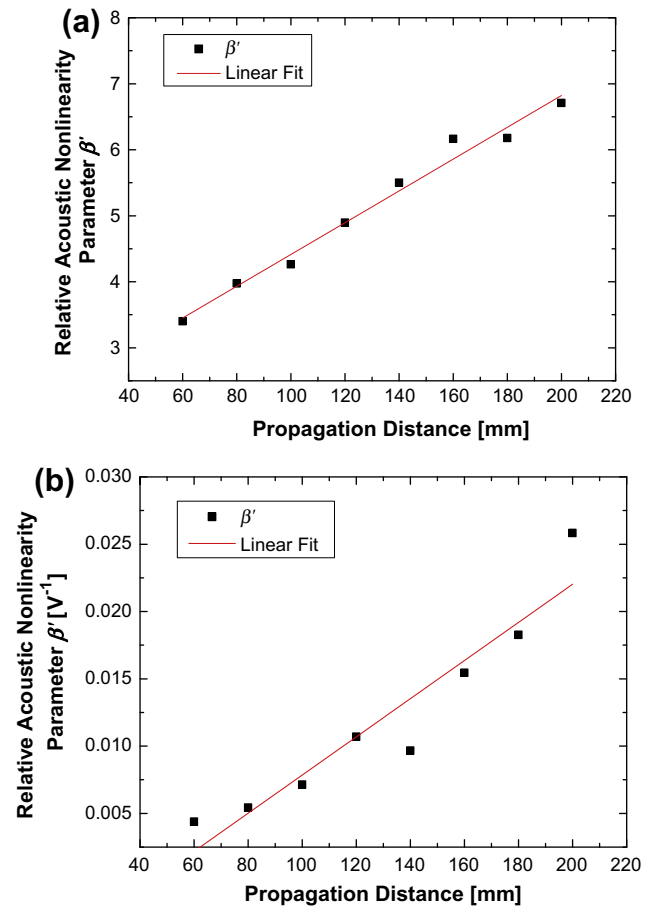
Fig. 7. An intact aluminum plate with eight sensing paths $A – S_i$ ($i = I, II, \ldots, VIII$): (a) schematic diagram (in *mm*); (b) PZT model for actuator; and (c) specimen in experiment.

Fig. 8. Relative acoustic nonlinearity parameter β' vs. wave propagation distance from (a) modeling and (b) the experiment.

between the two relationships in Fig. 8 has validated the developed modeling technique.

5.2. β' vs. sensing path offset

Ultrasonic Lamb waves propagating in an aluminum plate with a fatigue crack was examined using the developed modeling technique, complemented with experimental validation. Since a fatigue crack was introduced, the plasticity-driven nonlinearity and CAN were taken into consideration in the modeling, as explained in Section 2. Through this investigation, it is desired to establish a quantitative relation between β' of each sensing path and its offset distance from the fatigue crack.

A 6061 aluminum plate ($400 \times 240 \times 4.5 \text{ mm}^3$) was modeled, as shown schematically in Fig. 9a. A triangular notch of 15 mm by 25 mm was presumed at the center of the upper edge, consistent with the following experiment configuration, to serve as a fatigue crack initiator. A 4-mm long surface crack with 2.25 mm in depth and a uniform initial clearance of zero between the two crack surfaces (*viz.*, the two surfaces of the fatigue crack were initially in contact with each other) was modeled, running in parallel with the plate width from the tip of the notch. Ten circular PZT wafers, each with a 5-mm nominal diameter and a 0.5-mm thickness, were allocated on the same side of the plate. Five sensing paths $A_i – S_i$ ($i = I, II, \ldots, V$), each 200-mm long, were hence configured, all of which were perpendicular to the crack orientation. The offset distance d_o (defined in Fig. 9b) from the middle point of the fatigue crack to each sensing path was 0, 10, 20, 30, and 40 mm, respectively.

In analogy with the first case study, modeling procedures including meshing, material definition, signal acquisition, and dynamic simulation were recalled. For the material definition associated with a certain degree of plastic deformation in the neighborhood of the crack, the following representative values were used in the simulation, with a reference to the data given in [29], to estimate the local nonlinearity parameter using Eq. (8): $\Omega = R = 0.33$, $b = 0.286$ nm, $\Lambda = 1 \times 10^{15} \text{ m}^{-2}$, and $h = 5.4$ nm.
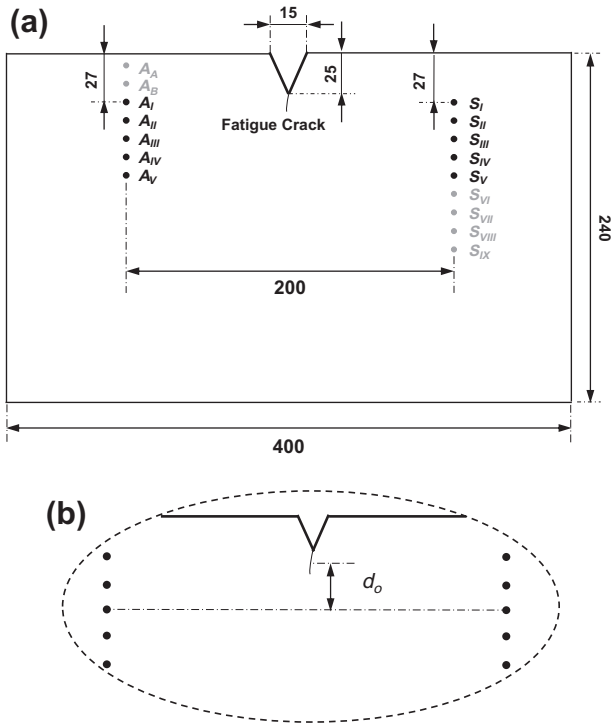
Fig. 9. (a) Schematic diagram of an aluminum plate with a fatigue crack initiator (in mm) (PZT wafers A_i – S_i (i = I, II, ..., V) for initial testing, and additional wafers A_A, A_B, and S_j (j = VI, VII, VIII, IX) for further investigation in Section 5.3) and (b) definition of d_o (crack length exaggerated).

In addition, CAN was added in the modeling because of the inclusion of the physical crack. Sixteen-cycle Hann-windowed sinusoidal tone bursts of 800 kHz were excited (considering the plate thickness). This prolonged excitation duration, compared with the five cycles used previously, was aimed at achieving a compromise between clear separation of different wave packets within the propagation distance of 200 mm and explicit recognition of second harmonic generation (as the cycle number of tone bursts increase, the wave bandwidth is reduced, the signal energy is more concentrated near the excitation frequency, the peak amplitude increases, and accordingly wave dispersion is minimized, all together benefiting the recognition of second harmonic [30]).

In the experiment, a 6061 aluminum plate of the same dimensions and the same PZT configuration as those in modeling was tested. The specimen had first undergone a HCF test on a MTS fatigue platform, subject to a sinusoidal tensile load at 5 Hz with a magnitude of 10 kN. After approximately 200,000 cycles, a barely visible fatigue crack was produced, measuring 4 mm in length and half of the plate thickness in depth, running from the notch tip and roughly paralleling the plate width. Ten PZT wafers of 5 mm diameter were attached to the plate in line with Fig. 9a, only after completion of the fatigue testing, to avoid possible degradation in adhesive layers during the fatigue processing. The ultrasonic testing was then carried out in accordance with the experimental procedure described in the previous case study.

Upon signal processing using STFT, β' for each sensing path was calculated and normalized with respect to the value acquired from path A_I – S_I, as displayed in Fig. 10, where the normalized β' against the offset distance obtained from the simulation and from the experiment are compared. In order to make the discussion applicable to general scenarios of arbitrary frequency-thickness products, d_o is normalized with respect to the probing wavelength λ. The two curves in Fig. 10 agree with one another quantitatively, with the greatest error less than 9%, corroborating the effectiveness of the modeling approach.

The relationship of β' vs. d_o/λ implies that the largest value of β' takes place when the sensing path just passes through the fatigue crack (i.e., A_I – S_I); while β' drops rather quickly as d_o/λ increases to 1.8 (corresponding to d_o = 10 mm), the decrease slows down as d_o/λ reaches 3.6 (corresponding to d_o = 20 mm). Beyond this point, β' decreases gradually to approximately 40% of its largest magnitude and no considerable change can be observed after d_o/λ reaches 5.5 (d_o = 30 mm).

5.3. Varied incidence angle and wave propagation distance

Note that the relationship of β' vs. d_o/λ presented in Fig. 10 was determined when the sensing path was perpendicular to the crack with a fixed path length of 200 mm. Pursuant to this, β', subject to varied incidence angles of probing waves and distinct propagation distances, was interrogated in FE simulation.

Dynamic simulation was conducted using the developed modeling technique, with additional PZT wafers introduced to the model as indicated by actuators A_A, A_B, and sensors S_{VI}, S_{VII}, S_{VIII}, S_{IX} in Fig. 9a, which formed another set of sensing paths of different incidence angles. The angle was varied from 90° (e.g., path A_I – S_I) to 84.3° (e.g., path A_B – S_{II}), and further to 78.7° (e.g., path A_A – S_{III}). For each incidence angle, the path lengths and the offset increment
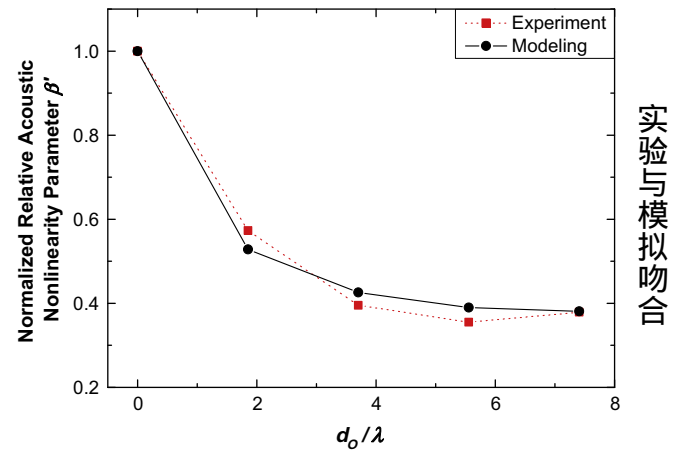
Fig. 10. Normalized relative acoustic nonlinearity parameter β' vs. d_o/λ (normalized offset distance with regard to probing wavelength λ) from both modeling and the experiment.
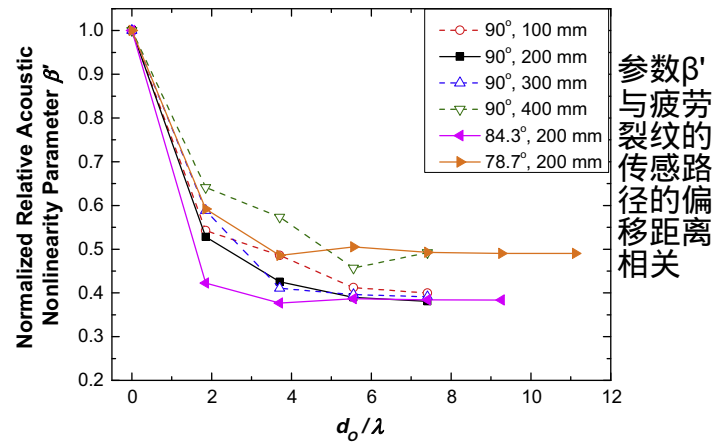
Fig. 11. Comparison of β' – d_o/λ curves at different incidence angles of probing waves (solid lines) and at different propagation distances (dashed lines) determined from the simulation data.

were kept consistent at approximately 200 mm and 10 mm, respectively, as in the previous case. Fig. 11 displays the relation of β' vs. d_o/λ obtained accordingly. It is interesting to note that no substantial variations can be obverted in terms of the trend of the curves when the incident angle varies. All these curves show that in the nearest region of the crack, there is a 40–60% drop in β'; beyond the point of $d_o/\lambda = 3.6$, the change in β' can be regarded as insignificant, in line with the observations in Fig. 10.

In addition to the effect of incidence angle, the dependence of β' on the length of the sensing path was also investigated. The path lengths were varied in the modeling from 100 to 400 mm in an increment of 100 mm, and their results are compared in Fig. 11. Once again, there are no considerable variations among the results: the largest β' always occurs at $d_o = 0$, and the decrease tends to slow down once beyond the point where $d_o/\lambda = 3.6$. This finding echoes the previous statement that local nonlinearity due to fatigue damage (β_l) is more dominant in introducing nonlinear distortion to ultrasonic waves, compared to its global (material) counterpart (β_g).

The curves shown in Figs. 10 and 11 collectively corroborate a reliable relationship between the relative acoustic nonlinearity parameter and the offset distance of sensing paths in a sensor network. With an incidence angle change of up to approximately ±10° from orthogonality and a wide range of propagation distance, β' depends exclusively on the offset distance of the sensing path from the fatigue crack. This conclusion can be especially helpful in locating fatigue cracks in conjunction with the use of a sensor network.

6. Concluding remarks

Given the importance of fatigue crack characterization using nonlinear features of ultrasonic waves, a modeling technique to interpret the nonlinearities associated with material and fatigue damage is established. The modeling technique attempts to comprehend material, geometric, plasticity-driven, and contact acoustic nonlinearities that may contribute to the nonlinear distortion of ultrasonic wave propagation. Results from the simulation and the experiments show good consistency, both revealing that the defined relative acoustic nonlinearity parameter β' has a linear cumulative growth with wave propagation distance due to the material and geometric nonlinearities. It is also discovered that β' of a particular sensing path in the sensor network can be quantitatively related to its offset from the crack within a wide range of sensing path lengths and angles of incidence. Meanwhile, it is important to realize that, with the quantitative relation of β' vs. d_o/λ obtained, the methodology established in this study shows a great potential to accommodate the demands of embeddable structural health monitoring. In practice, this technique would not need a baseline signal, and is not affected by extra nonlinearities such as those from instrumentation, making it tempting for the localization of fatigue cracks using a PZT sensor network.

Acknowledgements

References

[1] J.E. Michaels, T.E. Michaels, Detection of structural damage from the local temporal coherence of diffuse ultrasonic signals, IEEE Trans. Ultrason. Ferroelectr. Freq. Control 52 (2005) 1769–1782.
[2] T. Kundu, H. Nakatani, N. Takeda, Acoustic source localization in anisotropic plates, Ultrasonics 52 (2012) 740–746.
[3] H. Sohn, S.J. Lee, Lamb wave tuning curve calibration for surface-bonded piezoelectric transducers, Smart Mater. Struct. 19 (2010) 015007.
[4] A.J. Croxford, J. Moll, P.D. Wilcox, J.E. Michaels, Efficient temperature compensation strategies for guided wave structural health monitoring, Ultrasonics 50 (2010) 517–528.
[5] J.-B. Ihn, F.-K. Chang, Pitch-catch active sensing methods in structural health monitoring for aircraft structures, Struct. Health Monit. 7 (2008) 5–19.
[6] L. Yu, G. Bottai-Santoni, V. Giurgiutiu, Shear lag solution for tuning ultrasonic piezoelectric wafer active sensors with applications to Lamb wave array imaging, Int. J. Eng. Sci. 48 (2010) 848–861.
[7] P. Kudela, W. Ostachowicz, A. Zak, Damage detection in composite plates with embedded PZT transducers, Mech. Syst. Signal Pr. 22 (2008) 1327–1335.
[8] Z. Su, X. Wang, L. Cheng, L. Yu, Z. Chen, On selection of data fusion schemes for structural damage evaluation, Struct. Health Monit. 8 (2009) 223–241.
[9] J.-Y. Kim, L.J. Jacobs, J. Qu, Experimental characterization of fatigue damage in a nickel-base super alloy using nonlinear ultrasonic waves, J. Acoust. Soc. Am. 120 (2006) 1266–1273.
[10] M. Deng, J. Pei, Assessment of accumulated fatigue damage in solid plates using nonlinear lamb wave approach, Appl. Phys. Lett. 90 (2007) 121902.
[11] D. Dutta, H. Sohn, K.A. Harries, P. Rizzo, A nonlinear acoustic technique for crack detection in metallic structures, Struct. Health Monit. 8 (2009) 251–262.
[12] C. Pruell, J.Y. Kim, J. Qu, L.J. Jacobs, Evaluation of fatigue damage using nonlinear guided waves, Smart Mater. Struct. 18 (2009) 035003.
[13] C. Zhou, M. Hong, Z. Su, Q. Wang, L. Cheng, Evaluation of fatigue cracks using nonlinearities of acousto-ultrasonic waves acquired by an active sensor network, Smart Mater. Struct. 22 (2013) 015018.
[14] B.C. Lee, W.J. Staszewski, Lamb wave propagation modelling for damage detection: I. Two-dimensional analysis, Smart Mater. Struct. 16 (2007) 249–259.
[15] G. Zumpano, M. Meo, A new nonlinear elastic time reversal acoustic method for the identification and localisation of stress corrosion cracking in welded plate-like structures – a simulation study, Int. J. Solids Struct. 44 (2007) 3666–3684.
[16] O. Bou Matar, P. Guerder, Y. Li, B. Vandewoestyne, K. Van Den Abeele, A nodal discontinuous Galerkin finite element method for nonlinear elastic wave propagation, J. Acoust. Soc. Am. 131 (2012) 3650–3663.
[17] A.N. Norris, Finite-amplitude waves in solids, in: M.F. Hamilton, D.T. Blackstock (Eds.), Nonlinear Acoustics, Academic Press, San Diego, 1998, pp. 263–277.
[18] Z. Qian, Nonlinear Acoustics, second ed., Science Press, Beijing, 2009.
[19] L.D. Landau, E.M. Lifshitz, Theory of Elasticity, 3rd ed., Pergamon Press, Oxford, 1986.
[20] W.J.N. de Lima, M.F. Hamilton, Finite-amplitude waves in isotropic elastic plates, J. Sound Vib. 265 (2003) 819–839.
[21] R.T. Smith, R. Stern, R.W.B. Stephens, Third-order elastic moduli of polycrystalline metals from ultrasonic velocity measurements, J. Acoust. Soc. Am. 40 (1966) 1002–1008.
[22] S.M. Liu, S. Best, S.A. Neild, A.J. Croxford, Z. Zhou, Measuring bulk material nonlinearity using harmonic generation, NDT E. Int. 48 (2012) 46–53.
[23] A. Manonukul, F.P.E. Dunne, High- and low-cycle fatigue crack initiation using polycrystal plasticity, Proc. R. Soc. Lond. A 460 (2004) 1881–1903.
[24] C. Bermes, Generation and detection of nonlinear Lamb waves for the characterization of material nonlinearities, MS thesis, Georgia Institute of Technology, 2006.
[25] K. Kawashima, R. Omote, T. Ito, H. Fujita, T. Shima, Nonlinear acoustic response through minute surface cracks: FEM simulation and experimentation, Ultrasonics 40 (2002) 611–615.
[26] K.-Y. Jhang, Nonlinear ultrasonic techniques for nondestructive assessment of micro damage in material: a review, Int. J. Precis. Eng. Man. 10 (2009) 123–135.
[27] Y. Xiang, M. Deng, F.-Z. Xuan, C.-J. Liu, Experimental study of thermal degradation in ferritic Cr–Ni alloy steel plates using nonlinear Lamb waves, NDT E. Int. 44 (2011) 768–774.
[28] Z. Su, L. Ye, An intelligent signal processing and pattern recognition technique for defect identification using an active sensor network, Smart Mater. Struct. 13 (2004) 957–969.
[29] J. Cantrell, Substructural organization, dislocation plasticity and harmonic generation in cyclically stressed wavy slip metals, Proc. R. Soc. Lond. A 460 (2004) 757–780.
[30] Z. Su, C. Yang, N. Pan, L. Ye, L.-M. Zhou, Assessment of delamination in composite beams using shear horizontal (SH) wave mode, Compos. Sci. Technol. 67 (2007) 244–251.